

An Experimental Investigation of Fracture by Cavitation of Model Elastomeric Networks

ANTONELLA CRISTIANO,¹ ALBA MARCELLAN,¹ RONG LONG,² CHUNG-YUEN HUI,² JAN STOLK,³ COSTANTINO CRETON¹

¹Laboratoire de Physico-Chimie des Polymères et Milieux Dispersés, UMR7615, ESPCI ParisTech-CNRS-UPMC, 10 Rue Vauquelin, 75231 Paris Cédex 05, France

²Department of Theoretical and Applied Mechanics, Cornell University, Ithaca, New York 14853

³DSM Research, P.O. Box 18, 6160 MD Geleen, The Netherlands

Received 17 November 2009; revised 15 March 2010; accepted 25 March 2010

DOI: 10.1002/polb.22026

Published online in Wiley InterScience (www.interscience.wiley.com).

ABSTRACT: A new methodology to investigate the failure of elastomers in a confined geometry has been developed and applied to model end-linked polyurethane elastomers. The experimental *in situ* observations show that the elastomers fail by the growth of a single cavity nucleated in the region of maximum hydrostatic stress. Tests carried out at different temperatures for the same elastomer show that the critical stress at which this crack grows is not proportional to the Young's modulus E but depends mainly on the ratio between the mode I fracture energy G_{IC} and E . A reasonable fit of the data can be

obtained with a model of cavity expansion by irreversible fracture calculating the energy release rate by finite elements with a strain hardening constitutive equation. Comparison between different elastomers shows that the material containing both entanglements and crosslinks is both tougher in mode I and more resistant to cavitation relative to its elastic modulus. © 2010 Wiley Periodicals, Inc. *J Polym Sci Part B: Polym Phys* 48: 1409–1422, 2010

KEYWORDS: elastomers; fracture; mechanical properties

INTRODUCTION When elastomers are loaded under a nearly hydrostatic tensile stress, failure generally occurs by the formation of cavities. This phenomenon often called cavitation in the literature is of great practical interest since rubbers are often loaded in confined geometries, for example, in coatings or in the vicinity of particles in highly filled rubbers. Also, a dilatant stress of considerable magnitude is set up at the tip of a sharp crack.¹

Yet, the details of the cavity nucleation and growth are still poorly understood and a reliable cavitation criterion based on material properties is still lacking. A variety of models have been proposed to describe the expansion of a pre-existing cavity as a function of the elastic properties of the material, its surface tension, or its fracture toughness.^{2–12} However, experimental studies in well-controlled conditions have been much less available to the theoretical community. It is the goal of this study to investigate experimentally and for materials with a well-defined molecular structure, the fracture of simple elastomer networks in nearly hydrostatic tension.

The earliest documented evidence of the cavitation process is rather old^{13,14} and experiments were carried out with commercial rubbers (neoprene and natural rubber) using a relatively confined geometry called “poker-chip.” The rubber

disks were glued to a cylindrical sample holder and stretched in the thickness direction. Both studies observed that the stress–strain curve obtained in that geometry showed a marked and irreversible softening above a well-defined value of stress and noted that the fracture surfaces after failure contained the evidence of what they called “internal cracks” or macroscopic cavities.

Some years later Gent and Lindley¹⁵ used the same “poker-chip” geometry on natural rubber formulations to carry out their widely known systematic investigation. They prepared vulcanized rubber disks of identical diameter and different thicknesses varying therefore the aspect ratio (i.e., level of confinement). They found that the critical stress (defined as the inflection point in the stress–strain curve) decreased as the test-piece thickness was increased from very small values, becoming substantially constant for moderately thick samples. Postmortem observations showed that a series of small internal cracks were formed in the thin disks (uniformly distributed across the section), and only one or two large cracks were formed in the center in moderately thick disks. The most important observation of that study was that the fracture strength of the poker-chip samples appeared to be a reproducible material constant proportional to the elastic modulus. This certainly brought Gent and

Additional Supporting Information may be found in the online version of this article. Correspondence to: A. Marcellan (E-mail: alba.marcellan@espci.fr) or C. Creton (E-mail: costantino.creton@espci.fr)

Journal of Polymer Science: Part B: Polymer Physics, Vol. 48, 1409–1422 (2010) © 2010 Wiley Periodicals, Inc.

Lindley to name this internal cracking process a cavitation process and to model it as a simple deformation process (i.e., independent of initial cavity size) rather than as a fracture process.

They used the elastic theory of cavity inflation developed by Green and Zerna¹⁶ for neoHookean behavior to justify that the apparent yield point in the stress–strain curve appeared when the local hydrostatic pressure reached a critical value of $5E/6$ (where E is the small strain Young's modulus of the rubber).

This criterion of critical pressure was also confirmed by the studies of Cho and Gent¹⁷ using layers of transparent silicone rubber bonded to two steel balls or to two parallel steel cylinders. Upon loading, an inflection point appeared in the stress–strain curve when the applied stress reached a value of the order of the Young's modulus E , and optical observations showed concomitantly the presence of large cavities in the rubber layers. For thinner layers (layer thickness less than 5% of sphere diameter), two interesting effects were observed: in a continuous tensile test, the critical stress increased markedly above the elastic modulus, and if the load was instead kept constant just below the critical value, cavities appeared over time. These two results seem to indicate that the material is in a metastable state when the applied stress exceeds the small strain elastic modulus.

Experiments with rigid spherical inclusions have also been performed and reported in the literature, to characterize cavitation phenomena. Some earlier studies used samples of transparent polyurethane with rigid spherical inclusions^{18,19} and observed that cavities appeared at the edge of the inclusion due to the local high-triaxial stress there. They performed experiments with different types of polyurethanes and found a strong correlation between the critical stress and the modulus.

In conclusion, existing evidence shows a strong correlation between the critical stress (i.e., described from a change in stiffness) and the elastic modulus of the rubber, whereas postmortem observations and common sense point to a fracture process which should introduce the idea of defect size and should not be necessarily proportional to the modulus. This apparent discrepancy has been pointed out theoretically^{20,21} but never really verified experimentally.

The difficulty of studying cavitation experimentally lies mainly in the control of the stress field in nearly hydrostatic conditions, since this requires a reproducible and well-controlled confined geometry. The flat-to-flat geometry (“poker-chip”) for producing cavitation samples has been the most commonly used geometry reported in the literature. The main reason to use the poker-chip geometry is to introduce a large hydrostatic tension component in the sample. Furthermore, the incompressibility of the rubbery materials, which usually undergo large deformations during testing, is limited to relatively small strains before failure. This provides the benefit that the infinitesimal elasticity theory can be used in the analytical work without introducing large

errors. In this study, the choice of the experimental geometry was guided by the dual goal to minimize multiple cavitation (possibly to focus on a single cavitation event near the center of the sample) and to avoid alignment problems. A sphere-to-flat geometry was used to obtain a moderate confinement of the elastomer. The designed geometry for the study was chosen and fixed at the following degree of confinement: a ratio $h/R = 0.055$ and $a/h = 10$ where h is the minimum separation between the sphere and the flat, R is the radius of curvature of the sphere, and a is the diameter of the elastomer sample.

The elastomers chosen were unfilled and fully transparent model polyurethanes²² synthesized directly in the sample holder by end-linking monodisperse polypropylene glycol chains of different molecular weights with a triisocyanate. Perfect adhesion to the glass surfaces was obtained by covalent bonds. Special care was taken to obtain fully transparent bubble-free samples with a very well-controlled chemical structure and to investigate the effect of variations in chemical structure on the cavitation process, three specific model networks were selected: two monodisperse networks made, respectively, with short (unentangled) and long (entangled) precursor chains and a bimodal network made with a blend of long and very short chains. The rationale behind using a bimodal network composed of short and long chains was to obtain a network which would display a more pronounced strain hardening at lower levels of strain than a homogeneous network with an identical Young's modulus. In turn, we expected this feature to influence the resistance to cavitation based on Gent and Wang's theoretical predictions.²⁰

EXPERIMENTAL

PU Network Synthesis

The synthesis method was inspired by the protocol developed by Bos and Nusselder²² for similar polyurethanes.

The following chemicals were used without further purification: dry toluene (Aldrich); IRGANOX[®] 1035: sulfur containing primary (phenolic) antioxidant and heat stabilizer (kindly supplied by CIBA[®]). The following materials were purified before being used: ACCLAIM[®] 4200, Polyether Polyol with nominal molecular weight 4000 g/mol and ACCLAIM[®] 8200, Polyether Polyol with nominal molecular weight 8000 g/mol (kindly supplied by Bayer). POLY-G[®] 20-112 Urethane grade, Polyether diol, with nominal molecular weight 1000 g/mol (kindly supplied by Arch Chemicals); DESMODUR[®] RFE, solution of tris(*p*-isocyanatophenyl) thiophosphate in 27% of ethyl acetate (purchased from Bayer). Details of the purification procedure and the characterization of the reagents have been reported in a companion publication.²³

The networks were synthesized between glass plates (for the tensile and DMA samples), in cylindrical Teflon molds (for the compression tests) and in specially designed molds described later for the cavitation samples. In all cases, the reactive blend was prepared in the glove box, degassed, and poured in the mold. Then, curing of the samples was carried out in an oven under a nitrogen atmosphere. A first curing

TABLE 1 Composition of the Three PU Model Networks

Materials	Chain Extender	Crosslinker	Antioxidant	Experimental NCO/OH
PU4000	PPG 4000	tris(<i>p</i> -isocyanatophenyl) thiophosphate	0.1 wt % Irganox 1035	1.05
PU8000	PPG 8000			1.10
PU8000/1000	34 mol % PPG 8000 66 mol % PPG 1000			1.10

step of 48 h at 35 °C was carried out to increase viscosity in a controlled way to avoid macroscopic bubbles, followed by 80 h at 80 °C, for final network crosslinking. The networks were prepared at nearly stoichiometric conditions and with very low sol fractions, ensuring as defect-free as possible network structures.²³ Three different networks were synthesized and their composition is shown on Table 1.

Surface Treatments

For the cavitation tests, a perfect adhesion of the PU sample to the glass surfaces of the sample holder is essential. Because untreated glass did not adhere well to our PU samples, the surface of the glass had to be treated before sample casting. We used boro-silica glass plates of 40 mm in diameter and 3 mm in thickness, and plano-convex lenses of BK7 for optical uses (Melles Griot) with a radius of curvature of 18.2 mm (Fig. 1). The glass plates and the glass lenses were modified chemically by preparing self-assembled monolayers (SAMs). Before monolayer formation, the substrates were oxidized by immersion in a heated solution of piranha (blend of H₂SO₄ (96%) and H₂O₂ (30%) in 3:1 v/v) for 20 min at 150 °C, rinsed with Millipore water, and dried with a stream of nitrogen. Amino-terminated monolayers were prepared by immersion of the clean substrates in a 4% v/v solution of (3-Aminopropyl) triethoxysilane (purity ≥ 98%, Aldrich) in dry toluene, inside a gloves box (under nitrogen U atmosphere). After ~4 h, the substrates were rinsed with dry toluene inside the gloves box, and finally rinsed a second time with toluene (outside the gloves box) and dried under a stream of nitrogen. The surface-modified glass plates and glass lenses were then kept inside the gloves box until use.

To obtain lateral transparency of the samples, polished metallic side walls of the molds were designed in DURAL® (Aluminium alloy). These metallic side-walls had to be chemically modified to ensure demolding after crosslinking of the polyurethane networks. The polished metallic surfaces were first cleaned with acetone and dried during 30 min in

the oven at 120 °C. Fluoro-terminated monolayers were prepared by immersion of the clean and dry substrates in a 3% v/v solution of (Heptadecafluoro-1,1,2,2-tetrahydrodecyl) dimethylchlorosilane (ABCR) in dry toluene, inside a gloves box. After ~4 h, the substrates were rinsed first with dry toluene and then a second time with toluene and finally dried under a stream of nitrogen.

Mechanical Testing

Dynamic Mechanical Properties

The elastic modulus as a function of temperature and the glass transition temperature T_g were determined by DMA for each polyurethane network with a DMA model Q800 of TA instruments, used in tension mode. The frequency was set at 1 Hz and the amplitude around 0.1%, a temperature ramp of 2 °C/min was applied in a range of temperatures from -80 °C to 110 °C.

Tensile Tests

Tensile tests were performed on a standard tensile Instron machine (model 5565) equipped with a 10N load cell (with a relative uncertainty of 0.16% in the range from 0 to 0.1N) and with a video extensometer which follows the local displacements of two spots up to 120 mm with a relative uncertainty of 0.11% at full scale). Films of the PU were used to prepare the tensile samples by using a die-cutter with a dog-bone shape. The experiments were performed at an initial strain rate of $\sim 0.0067 \text{ s}^{-1}$ and at room temperature ($\sim 25 \text{ }^\circ\text{C}$).

Compression Tests

Uniaxial compression experiments were performed in a hydraulic MTS 810 machine with a load cell with a maximum capacity of 2.5 kN and a resolution of $\pm 0.5N$. The samples were cylinders ($d_0 = 5 \text{ mm}$ in diameter and $h_0 \sim 5 \text{ mm}$ in height).

The compression test consisted of an initial compressive contact to 1N to ensure a starting point of complete contact

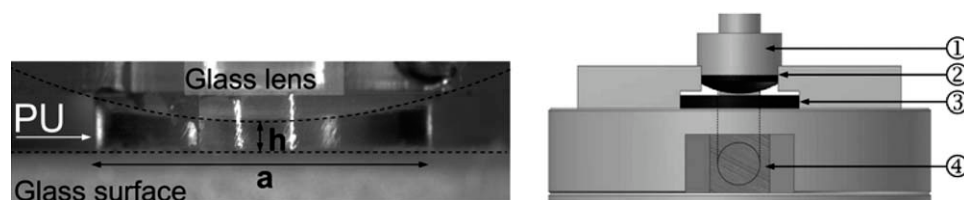


FIGURE 1 Picture of a cavitation sample and design of the sample holder. The PU sample is fixed between a glass plate and a glass lens ($a = 10 \text{ mm}$, $a/h = 10$, and the radius of curvature of the lens is $R = 18.2 \text{ mm}$). ① Metallic probe; ② Glass lens glued to the (polished) surface of the probe; ③ Glass plate; and ④ 45° mirror for the top view.

TABLE 2 Storage Modulus E' at 1 Hz of PU4000, PU8000, and PU8000/1000 as a Function of Temperature

Materials	$E'^{25\text{ }^\circ\text{C}}$ (MPa)	$E'^{50\text{ }^\circ\text{C}}$ (MPa)	$E'^{70\text{ }^\circ\text{C}}$ (MPa)	$E'^{100\text{ }^\circ\text{C}}$ (MPa)
PU4000	1.3 ± 0.08	1.38 ± 0.07	1.45 ± 0.09	1.55 ± 0.04
PU8000	0.8 ± 0.06	0.84 ± 0.03	0.88 ± 0.04	0.93 ± 0.04
PU8000/1000	1.2 ± 0.07	1.28 ± 0.04	1.35 ± 0.06	1.44 ± 0.05

between the sample and the glass surfaces. The interfaces between the sample and the glass plates were lubricated with a silicone oil to minimize friction and to obtain a homogeneous strain field. In this type of experiments, it is generally difficult to ensure that the boundary condition is truly full slip. We note, however, that the elastic modulus (in the Gaussian region) obtained in compression (see Figure S1 in the Supporting Information) is identical to that in tension and that the loading/unloading curves show minimal hysteresis. Both results imply that friction was minimized. The tests were performed at constant crosshead rate and at an initial compressive strain rate of 0.0067 s^{-1} . All the experiments were performed at room temperature ($\sim 25\text{ }^\circ\text{C}$).

Fracture

The fracture experiments were performed in the Double Edge Notch Tensile geometry (DENT) inside a DMA, model Q800 of TA instruments, in tension mode. The fracture toughness of the three polyurethane networks was measured at a nominal strain rate of $0.67\% \text{ s}^{-1}$ for different temperatures. All fracture experiments were carried out with samples bars with rectangular cross sections with dimensions of $4 \times 30 \times 1\text{ mm}^3$, using an initial gauge length around $L_0 \sim 15\text{ mm}$. For each sample, a 1-mm long notch was made on each side by using a razor blade. Exact length of the notch was checked by optical microscopy.

Cavitation

To perform the cavitation experiments, a specific sample holder has been designed. The main requirement was to have a quite stiff set-up with a very low compliance (with

this set-up the compliance was $10\text{ }\mu\text{m}/100\text{N}$). Other requirements were to have a good top and side view of the sample. Figure 1 presents side view pictures of the sample during testing.

The sample holder was then fixed to a hydraulic MTS810 tensile testing machine. Two cameras were used for a double visualization: a Marlin F-033B, standard camera (25 fps) with a resolution of $656 \times 494\text{ pix}$; and a Pulnix TM-6740 CL high speed camera (200 fps) with a resolution of $640 \times 480\text{ pix}$. During the mechanical test, the images acquired with a side and top views were synchronized with the force and displacement data acquisition. Five tests were typically performed for each experimental condition and material.

Mechanical Properties of the Networks

Table 2 summarizes the storage moduli E' measured by DMA at 1 Hz at the four test temperatures. The observed increase in modulus with temperature is typical of the thermoelastic behavior which dominates the response of unfilled elastomers. It is a telling sign of the very homogeneous and defect free character of the network, since any significant chain relaxation would have led to a modulus staying constant or even decreasing with temperature. This is particularly true at such low strains (below 0.1%) where entropic elasticity is not expected to dominate as much. A more detailed characterization of the model networks is reported in a separate article.²³

Figure 2(a) shows typical tensile test results for the three polyurethane networks. All three curves are markedly

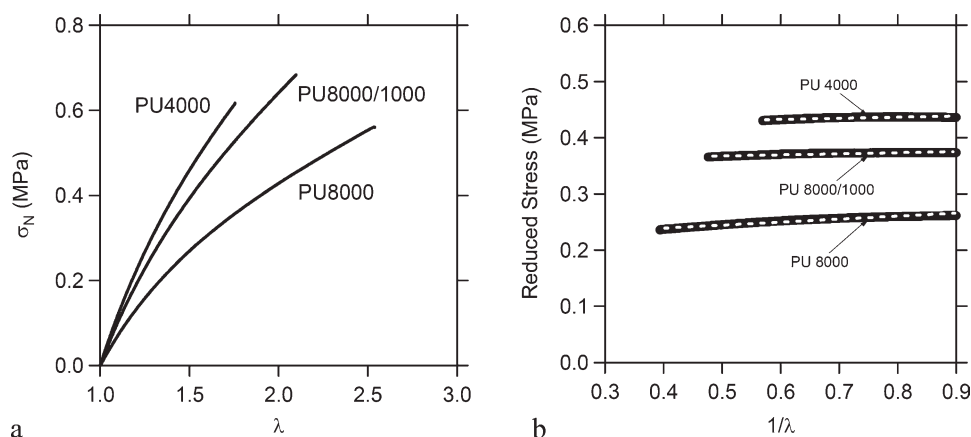


FIGURE 2 Uniaxial extension (Room Temperature— $\dot{\epsilon} = 0.0067\text{ s}^{-1}$): (a) Nominal stress versus λ , for the three polyurethane model networks and (b) the comparison of corresponding experimental data plotted as reduced stress versus $1/\lambda$ with the best fits of the Rubinstein and Panyukov' model.

TABLE 3 Parameters of the Rubinstein and Panyukov' Model from the Best Data Fit

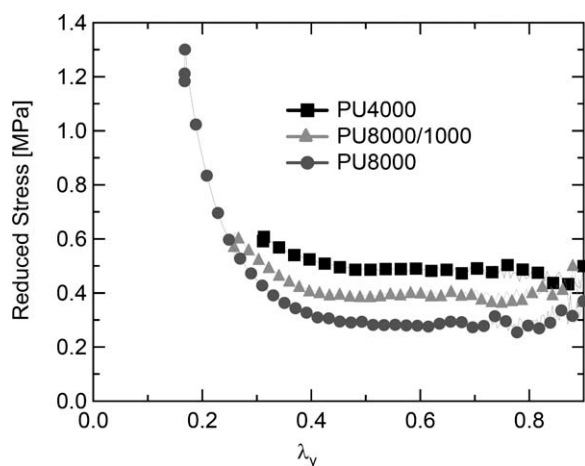
Materials	G_c (MPa) Crosslink Contribution	G_e (MPa) Entanglement Contribution
PU4000	0.44	0.001
PU8000	0.20	0.050
PU8000/1000	0.37	0.010

nonlinear and show softening but no obvious evidence of strain hardening is visible. All three materials break at moderate extension values and the maximal extension values scale inversely with the initial modulus. Fracture is brittle with an unstable crack propagation in all cases. Differences between the three network structures are more apparent on Figure 2(b) which plots the reduced stress σ_R , defined as follows:

$$\sigma_R = \frac{\sigma_N}{(\lambda - 1/\lambda^2)} \quad (1)$$

as a function of the stretch ratio λ in the tension test. In eq 1, σ_N is the nominal stress. The softening is most marked for the PU8000 and is non-existent for the PU4000. It is possible to fit the tensile data for these model networks with the Rubinstein-Panyukov model²⁴ which separates the entanglement and crosslink contributions to the modulus and results are given in Table 3.

The strain hardening behavior was not observed in tensile measurements because catastrophic failure occurred at low levels of strain. To characterize the large strain behavior, uniaxial compression tests, which are equivalent in terms of strain field to equibiaxial stretching tests, were also carried out. Figure 3 shows the reduced stress in uniaxial compression versus λ_y for the three networks. The clear upswing in reduced stress at low values of λ_y can be observed for the three materials.

**FIGURE 3** Uniaxial compression behavior (Room Temperature, $\dot{\epsilon} = 0.0067 \text{ s}^{-1}$) for the three polyurethane model networks plotted as reduced stress versus λ_y .

Although several strain hardening constitutive equations for rubbers have been proposed and could have been used to fit the data, we chose an exponentially hardening model used by Seitz et al.²⁵ because it was easily adaptable to finite element simulations without divergence problems. The strain energy density, U is expressed as follows:

$$U = \frac{E}{6} J^* \left(\exp\left(\frac{J_1}{J^*}\right) - 1 \right); \quad J_1 = \lambda_x^2 + \lambda_y^2 + \lambda_z^2 - 3 \quad (2)$$

where E is the small strain Young's modulus and λ_x , λ_y , and λ_z are the principal extension ratios and J^* the maximal extensibility parameter. For uniaxial experiments, The x and z directions are equivalent so $\lambda_x = \lambda_z = \lambda_y^{-1/2}$ and the nominal stress (σ_N) can be readily obtained by deriving the strain energy function with respect to λ_y , which gives for the strain energy function given in (2):

$$\sigma_N = \frac{E}{3} \left(\lambda_y - \frac{1}{\lambda_y^2} \right) \exp\left(\frac{J_1}{J^*}\right); \quad J_1 = \lambda_y^2 + \frac{2}{\lambda_y} - 3 \quad (3)$$

This model has only two free fitting parameters, J^* the maximal extensibility parameter (fitted from compression data) and E , the Young's modulus (fitted from the small strain tensile behavior). At small strains, the model reduces to the Neo-Hookean model. At larger strains, the finite extensibility of the chains is accounted for by J^* in a way that is similar to a model proposed by Gent.²⁶

Fits of the data are given in the Supporting Information (Fig. S1) and are quite good for both experiments implying that our lubricated compression experiments have been carried out properly. Table 4 shows the value of the best-fit parameters.

The comparison between the three materials is, however, a bit surprising. In principle, the looser the network mesh and the higher J^* should be. However, the values of J^* that have been found from the experimental curves shown in Figure 3, both suggest the opposite conclusion. A possible explanation is that the most reliable value is that obtained for the PU8000, given the significantly broader range of experimental data used for the fit as can be seen on Figure 3. It is likely that the other two networks have experienced some damage during the compression test without catastrophic fracture.

To complete the mechanical characterization of the networks, we carried out fracture toughness tests in mode I with a

TABLE 4 Best-Fit Parameters of the Exponential Model (eq 3): J^* the Maximal Extensibility Parameter Fitted from Compression Data and E , the Young's Modulus Fitted from the Small Strain Tensile Behavior

Materials	E (MPa)	J^*
PU4000	1.17 ± 0.01	9.26 ± 0.70
PU8000	0.69 ± 0.02	5.62 ± 0.36
PU8000/1000	0.98 ± 0.02	7.37 ± 0.34

TABLE 5 Mode I Fracture Energy G_{IC} Obtained for the Three Polyurethane Model Networks, at 25 °C and $\dot{\epsilon} = 0.006 \text{ s}^{-1}$ and Calculated Lake and Thomas Threshold G_0 Values

Materials	$G_{IC}^{25 \text{ °C}} (\text{J m}^{-2})$	$G_{IC}^{50 \text{ °C}} (\text{J m}^{-2})$	$G_{IC}^{70 \text{ °C}} (\text{J m}^{-2})$	$G_{IC}^{100 \text{ °C}} (\text{J m}^{-2})$	$G_0 (\text{J m}^{-2})$
PU4000	136 ± 5	104 ± 4	60 ± 4	41 ± 4	11.8
PU8000	252 ± 4	140 ± 6	106 ± 7	66 ± 3	17.5
PU8000/1000	145 ± 5	94 ± 5	58 ± 6	39 ± 2	12.5

double edge notch sample (DENT) at the temperatures where cavitation experiments were carried out. Results of these tests which have been discussed in detail elsewhere²³ are given in Table 5.

For all three networks, the fracture energy decreases significantly with T suggesting that the dissipative processes at the crack tip are of a viscoelastic nature. Even at 100 °C, there is no evidence of a plateau and it is not clear that a threshold value, in the sense of the Lake-Thomas model,²⁷ has been reached for the fracture toughness. Unfortunately, time constraints prevented us from carrying out more experiments at higher temperatures. Significant differences in toughness are observed between the networks even though glass transition temperatures are rather similar and all networks are very elastic at room temperature. It is clear that the entangled network (PU8000) is much tougher than the others at room temperature and this difference remains at all temperatures qualitatively consistent with the Lake-Thomas model of rub-

ber fracture.²⁷ The introduction of 20 wt % of short chains on the other hand considerably embrittles the PU8000 elastomer.

Cavitation Mechanisms

The core of this study is to investigate the details of fracture mechanisms of the elastomers in confined conditions. In the following sections, we will refer to this mechanism as cavitation by opposition to mode I fracture in unconfined conditions.

The synchronization of the force and time signal with two video cameras reveals the damage scenario of the confined rubber disk and we first present data obtained at room temperature for the different materials.

Figure 4 shows a typical curve of force versus displacement (obtained for PU4000) at 25 °C and $\dot{\epsilon} \sim 10^{-2} \text{ s}^{-1}$. The numbers correspond to the synchronized image acquisition

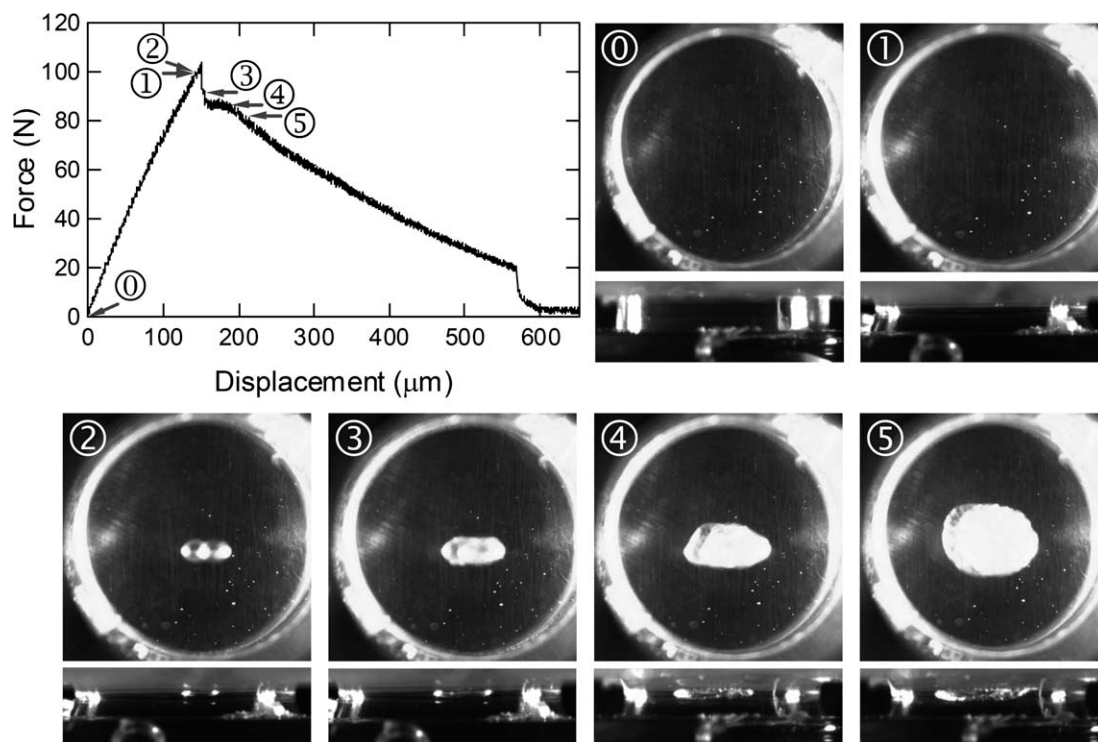


FIGURE 4 Force versus displacement plot of a typical cavitation experiment obtained for PU4000 at 25 °C and at $10 \mu\text{m s}^{-1}$, corresponding to a mean $\dot{\epsilon} \sim 10^{-2} \text{ s}^{-1}$, and synchronized images (top and lateral views). ①: ($t = 0 \text{ s}$, $F = 0 \text{ N}$); ②: ($t = 15.65 \text{ s}$, $F = 99.5 \text{ N}$); ③: ($t = 15.69 \text{ s}$, $F = 100 \text{ N}$); ④: ($t = 16.05 \text{ s}$, $F = 91.5 \text{ N}$); ⑤: ($t = 18.99 \text{ s}$, $F = 87 \text{ N}$); ⑥: ($t = 21.44 \text{ s}$, $F = 82.5 \text{ N}$).

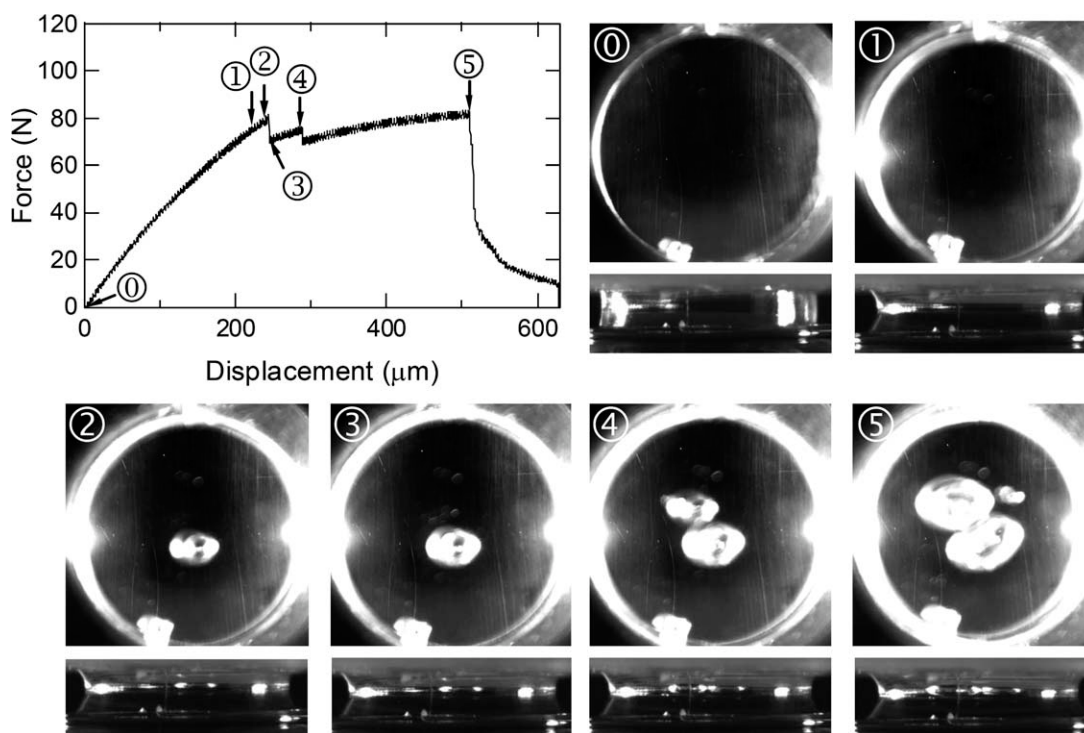


FIGURE 5 Force versus displacement plot of a typical cavitation experiment obtained for PU8000 at 25 °C and at $10 \mu\text{m s}^{-1}$, corresponding to a mean $\dot{\epsilon} \sim 10^{-2} \text{ s}^{-1}$, and synchronized images (top and lateral views). ①: ($t = 22.41 \text{ s}$, $F = 77 \text{ N}$); ②: ($t = 24.20 \text{ s}$, $F = 80 \text{ N}$); ③: ($t = 24.58 \text{ s}$, $F = 71 \text{ N}$); ④: ($t = 28.96 \text{ s}$, $F = 75.5 \text{ N}$); ⑤: ($t = 50.69 \text{ s}$, $F = 82.5 \text{ N}$).

(pictures taken from the top and lateral view). The synchronized images reveal the location, level of force and time, where cavities appear. Note that the resolution of the time measurement is of $\pm 40 \text{ ms}$ and the force is $0.5N$. The cavity is always growing in the bulk and not at the interface between the glass and the PU, as can be easily checked on the fracture surfaces.

As shown in Figure 4, the force versus displacement curve, in the initial part of the curve, from zero up to the maximal force F_{max} , the response of the confined sample can be considered as linear. Depending on conditions and materials, some small white spots can appear for relatively high values of forces below F_{max} without any detectable change in compliance. These white spots which appear very fast (time elapsed 40 ms between two consecutive images) and stop growing in size are presumably cracks opened from an optically invisible pre-existing defect. This first stage of cavity expansion can be estimated as an initial crack growth rate, from the time resolution of the camera, to be higher than 10–20 mm/s. This part of the crack growth process is unstable and the growth rate is limited by dissipative processes. Then, the second part of the curve, after the drop in force (F_{max}), corresponds to stable propagation of one single crack across the sample in confined conditions.

The maximum in force F_{max} is due to the fast expansion of one cavity, which we call the critical cavity, to a macroscopic size. This critical cavity is systematically located in the central region of the sample.

These two stages (i.e., first part of the force-displacement curve linear, followed by stable crack propagation) are observed for nearly all samples. However, their relative importance differs for the different networks and experimental conditions, as shown in Figure 6. The cavitation process in the PU8000 network (Fig. 5) appears slightly different from that observed for the nonentangled network PU4000, as shown in Figure 4. The second and third peaks in Figure 5

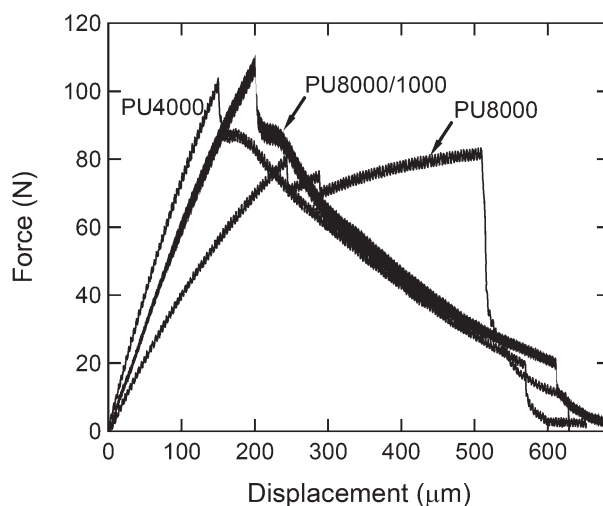


FIGURE 6 Typical force-displacement curves obtained for the three model PU networks at 25 °C and $10 \mu\text{m s}^{-1}$ (mean $\dot{\epsilon} \sim 10^{-2} \text{ s}^{-1}$).

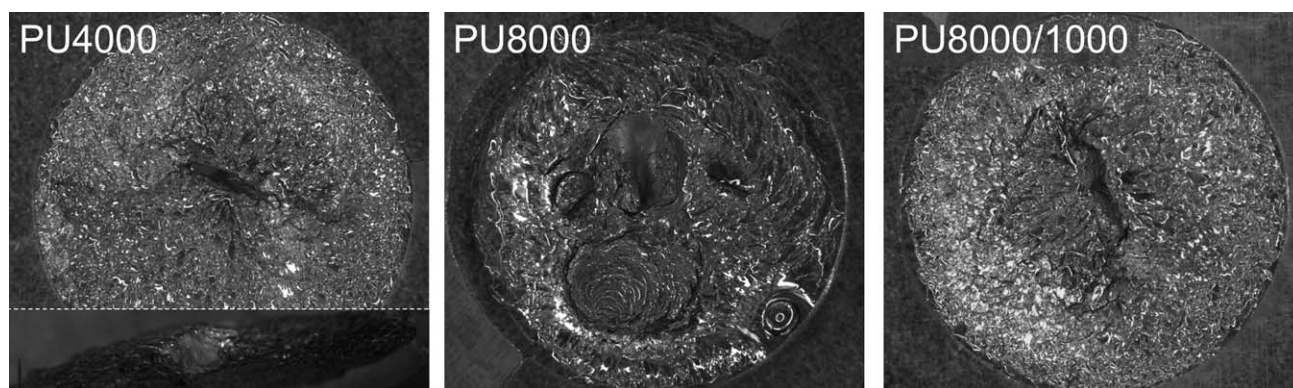


FIGURE 7 Typical fracture surfaces of PU4000, PU8000, and PU8000/1000 obtained by optical microscopy (scale is given by the mean diameter of the sample $a = 10$ mm).

correspond to two additional critical cavities growing at different locations; this can only happen if the first crack stops growing at a reasonably large size. Image 2 shows a stable critical cavity, followed by the propagation initiation of two additional critical cavities, seen, respectively, in images 4 and 5. Qualitatively, PU8000 appears to be more resistant to cavity growth relative to PU4000.

The mechanical response of the bimodal network PU8000/1000 is very similar to that of the PU4000: only one single critical cavity grows. The effect of adding 20 wt % of short chains (PPG1000) seems to cancel the stabilizing effect of having long chains (with entanglements) in terms of resistance to cavitation (i.e., maximum extension at fracture).

All three curves in Figure 6 are nonlinear, albeit less so than the uniaxial tensile curves shown in Figure 2, and the stiffness of the samples clearly scales with the modulus of the material. Some scatter of the slopes in the force versus displacement curves could be observed and can be attributed to the slight variations in experimental geometry (thickness h). The F_{\max} corresponding to a critical cavity growing, occurs at relatively low strain for all three PU model networks.

Fracture Surfaces

In the second stage of the fracture process, the displacement is increased and the central crack propagates inside out along a principal normal stress trajectory until the two pieces are completely apart. Figure 7 shows a typical micrograph of the fracture surfaces; we observe that the initial damage occurs in the central region of the sample, confirming that the cavity/cavities were in the bulk of the material and never at the elastomer/glass interface. The surface is also clearly very rough for all samples.

For PU4000, fracture initiation was very close to the center of the sample and a crack of ~ 1.5 – 2 mm long was first formed. By focusing closer in the central region of the fracture surface, we observe that the crack surface presents a radial step, inclined at an angle of $\sim 45^\circ$ – 90° relative to the plane of the glass plate, typically corresponding to the oval-

ity during fast cavity expansion, see Figure 4 in image 4. This first fast growth of a central crack is followed by a controlled fracture propagating outward. A similar morphology was observed for PU8000/1000.

As shown in Figure 6, the cavitation process is slightly different for the PU8000. The corresponding multiple critical cavities observed in the videos are present on the fracture surface as traces of three to four oyster-shaped cavities. Because the growth of the first cavity stops due to the toughness of the material, the stress keeps increasing as the material is deformed and several cavities can grow to a macroscopic size one after the other. It should be noted that as the crack grows, the degree of hydrostatic tension decreases. Since the energy release rate is very sensitive to the degree of triaxiality, it is possible that the crack slows down or even stops especially for tough materials.

Cavitation and Temperature Effect

Using the methodology exposed above, we characterized the cavitation resistance of our three model networks at room temperature (25°C) and at three other temperatures up to 100°C . The same crosshead speed $10\ \mu\text{m s}^{-1}$ (mean $\dot{\epsilon} \sim 10^{-2}\ \text{s}^{-1}$) was used for all conditions.

Figure 8 illustrates the typical mechanical response of our confined samples for temperatures between room temperature and 100°C . We observe that when the temperature is increased (100°C), the peak force always decreases and the shape of the curves changes. The propagation regime becomes much faster and less controlled as the temperature is increased. Although there are important differences between the materials at room temperature, raising the temperature considerably reduces the resistance to cavitation of all three materials and the differences become smaller.

Concerning the fracture surfaces, the same qualitative observations can be made at higher temperatures but in general, the growth of the critical cavity occurs faster and at lower forces at higher temperatures than at 25°C .

Figure 9 shows a comparison of the average projected diameter of the cracks as a function of time. Data is taken from a

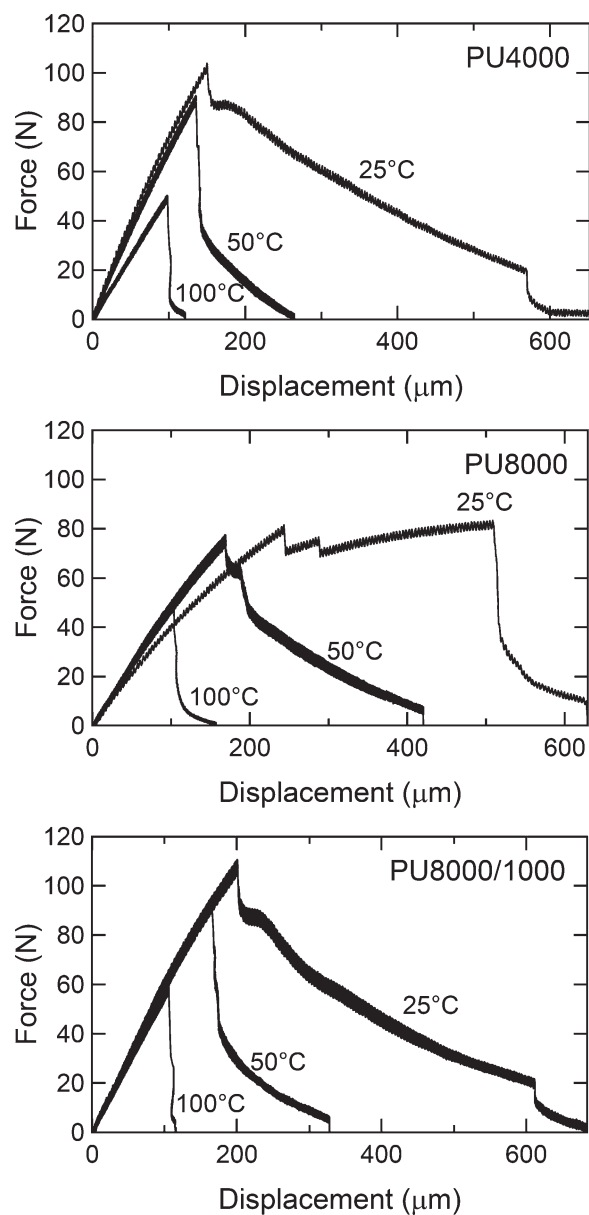


FIGURE 8 Typical force–displacement curves of the confined elastomers showing a lower critical force with increasing temperatures. Comparison at $10 \mu\text{m s}^{-1}$ (mean $\dot{\epsilon} \sim 10^{-2} \text{ s}^{-1}$), from 25 °C to 100 °C.

representative experiment. It appears that the cavity growth occurs faster at higher temperatures than at room temperature and the fastest fracture process occur at the highest temperature 100 °C, for the three polyurethane networks. The shape of the growing crack/cavity is also far from being spherical and details are given in the Supporting Information.

From F_{max} to P_c , the Local Hydrostatic Stress Calculation

Although for qualitative comparisons, the force–displacement curves are sufficient, a detailed comparison of the critical stress for cavity growth for different materials and temperatures, with existing theories of cavitation has to rely on a

local measure of the hydrostatic stress since the simplest criterion for the growth of a cavity is that of a critical value of the local hydrostatic stress.^{6,15,16}

The analytical solution for the relationship between force and local hydrostatic stress for the flat-to-flat geometry has been already reported in the literature,²⁸ but for the sphere-to-flat geometry, the solution had to be calculated with a Finite Element Method (FEM). The calculation was carried out in small strain with a compressible material and the details of the calculation and the method are given in the Supporting Information.

The outcome of the simulation is a calibration constant $C(a/h, R/h, \nu)$ relating the macroscopic force and the corresponding maximal hydrostatic stress $\sigma_{\text{hydrost}}^{\text{max}}$, localized at the center of the geometry in the vicinity of the sphere.

$$\sigma_{\text{hydrost}}^{\text{max}} = C(a/h, R/h, \nu)F_{\text{max}} \quad (4)$$

Since in our geometry the radius of the sphere, R and the diameter of the sample, a are fixed, this constant, C essentially depends on the degree of incompressibility (Poisson's ratio ν) and on the confinement of the sample (thickness, h). A value of the Poisson's ratio, $\nu = 0.49994$ was estimated from the shear modulus and bulk modulus of the elastomer and h was directly measured. In the range $0.8 \text{ mm} < h < 1.2 \text{ mm}$, the calibration factor C is then given by the following:

$$C = 0.0026 + 0.029h^{-0.041} \quad (5)$$

where h is in mm and C is in MPa/N . Note that C depends only slightly on h , as 5% change in layer thickness results in only a 2% change in calibration factor.

To define the local hydrostatic stress, each cavitation event was localized in the bulk of the sample, mainly occurring in the vicinity of the sphere; the position from the sample center (coordinate R) was used. The critical hydrostatic stress

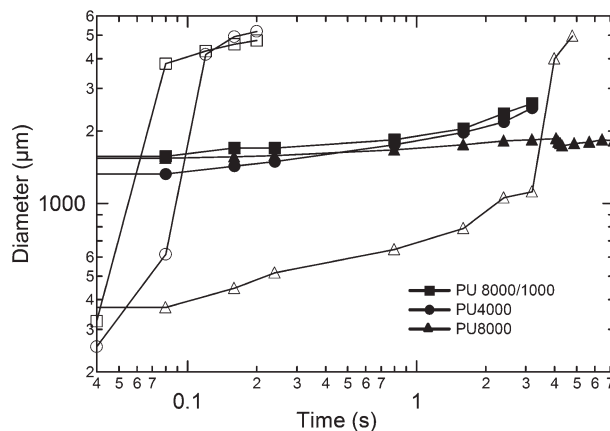


FIGURE 9 Average projected diameter of the cavity as a function of the time for two temperatures 25 °C (filled symbols) and 100 °C (unfilled symbols), ($10 \mu\text{m s}^{-1}$ mean $\dot{\epsilon} \sim 10^{-2} \text{ s}^{-1}$) for: PU4000, PU8000, and PU8000/1000.

TABLE 6 Local Critical Hydrostatic Stress P_c Obtained at for Different Temperature ($10 \mu\text{m s}^{-1}$, Mean $\dot{\epsilon} \sim 10^{-2} \text{ s}^{-1}$)

Materials	$P_c^{25^\circ\text{C}}$ (MPa)	$P_c^{50^\circ\text{C}}$ (MPa)	$P_c^{70^\circ\text{C}}$ (MPa)	$P_c^{100^\circ\text{C}}$ (MPa)
PU4000	3.25 ± 0.13	2.63 ± 0.06	2.62 ± 0.08	1.77 ± 0.07
PU8000	2.45 ± 0.08	2.09 ± 0.13	1.83 ± 0.10	1.64 ± 0.12
PU8000/1000	3.09 ± 0.15	2.66 ± 0.08	2.19 ± 0.15	1.77 ± 0.11

corresponding to the critical cavity expansion will be denoted by P_c .

P_c Versus Temperature: Toward an Expansion Model

Table 6 presents the calculated values of P_c , the critical local hydrostatic stress corresponding to the peak force, for the different temperatures and the three networks. Figure 10 shows graphically P_c as a function of the modulus for different temperatures and P_c/E as a function of temperature. It is clear that contrary to previous results,^{15,17} P_c is not proportional to the modulus and does not even scale with it. Figure 10(b) shows the ratio P_c/E as a function of the temperature for the three materials and provides a good overview of the data. Clearly, the pure long chain network PU8000 has higher cavitation strength relative to its modulus than the two other networks and that the ratio P_c/E decreases dramatically with temperature.

This interesting result provides some clues on the mechanism. Any mechanism purely based on reversible nonlinear elastic behavior will be unable to explain these results since nonlinear elastic properties are weakly dependent on the temperature and the modulus of entropic origin increases with temperature.

We also observe that the measured P_c at different temperatures is significantly higher than the predicted criterion of critical pressure $P_c = 5E/6$ for unstable expansion.^{15,16}

This is not surprising since the simple deformation model proposed by Green and Zerna¹⁶ was developed for neo-

Hookean materials, considering that the cavity was in an infinite medium growing by deformation at constant applied true stress and no surface tension. However, even accounting for surface tension in the deformation model, one cannot explain the temperature dependence of P_c . The next step is then to consider irreversible expansion by fracture.

The Griffith's fracture criterion²⁹ states that a crack will grow when the energy release rate " G " reaches the critical value G_c ($G \geq G_c$) also called fracture energy which is in principle a material constant, depending only on the mode of loading. Because the energy release rate depends on the initial flaw size, a given material can have different fracture stresses for the same value of G_c . In our geometry and although the size and shape of flaws initially present is unknown, we assume that a penny-shaped crack with initial radius r_0 much smaller than the sample size exists. Then, within the framework of linear elasticity, the dependence of the fracture energy G on the initial crack radius r_0 is given by the following²¹:

$$G \cong \frac{P^2}{E} r_0 \phi_{\text{geometry}} \tag{6}$$

where ϕ_{geometry} is a dimensionless function that involves the geometry, E is the Young's modulus of the hyperelastic material at small strains, and P is the hydrostatic stress. This expression remains of course valid at the critical value, i.e., when the hydrostatic stress P becomes P_c and G becomes G_c . Equation 6 should apply at low applied pressure, when the energy release rate G is given by the small strain theory.²¹

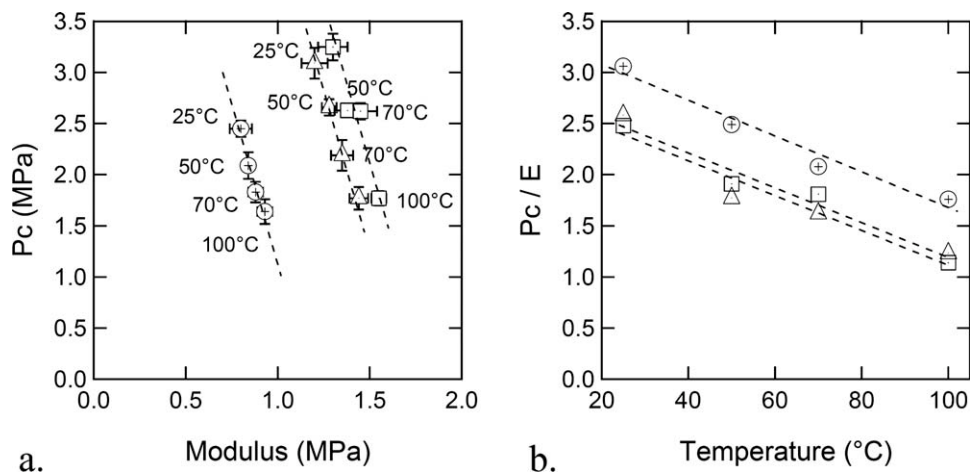


FIGURE 10 (a) Critical hydrostatic stress P_c as a function of the modulus at different temperatures. (b) Critical hydrostatic stress P_c normalized by the Young's modulus as a function of temperature. \circ PU8000, \square PU4000, Δ PU8000/1000; Dashed lines are a guide to the eye.

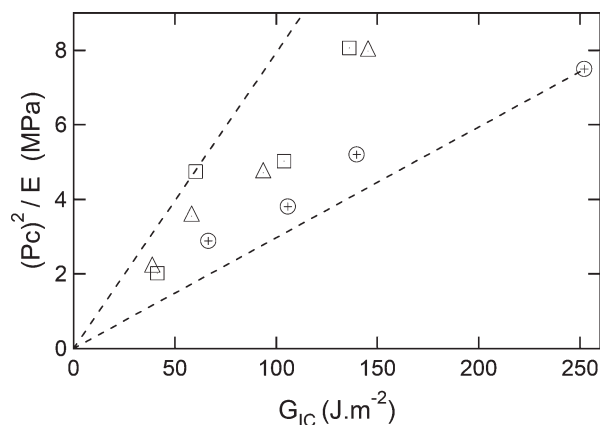


FIGURE 11 Expansion by fracture using linear elastic fracture mechanics (LEFM). Relation between P_c^2/E and G_{IC} for the three polyurethane model networks at different temperatures. ○ PU8000, □ PU4000, and △ PU8000-1000.

The DENT geometry used to perform fracture toughness experiments (Table 5) is clearly different than the confined geometry used to perform the cavitation experiments. Yet we can check whether P_c^2/E scales with G_{IC} measured in DENT tests. Figure 11 shows that for the same material at different temperatures the relationship between P_c^2/E and G_{IC} is approximately linear. If now we try to fit all the materials in one single line, we observe that it is not possible. This means that either r_0 (proportional to G based on eq 6) is different for each material or the fracture energy G as calculated by eq 6 is not good because Linear Elastic Fracture Mechanics (LEFM) does not take into account the limiting extension of the chains (strain hardening) as well as the large deformation to calculate the energy release rate. In this case, the results of Figure 11 suggest either that the linear theory overestimates G for the PU4000 and PU8000/1000 or that the value of G_c in the hydrostatic geometry is much higher than the DENT value again for the PU4000 and PU8000/1000.

The next step is then to use a nonlinear fracture model. To our knowledge, the first finite strain version of the Griffith argument for rubbers was proposed by Gent and Wang.²⁰

In Gent and Wang's model,²⁰ G is calculated by assuming from the start that a planar circular crack of radius r_0 under hydrostatic constant stress can expand to an initial spherical cavity of the same radius r_0 without any work. This is then the reference configuration and G is calculated by comparing the strain energy of two cavities of different initial radii expanded to the same volume. The advantage of this methodology is that if the constitutive equation is not too complicated, the energy release rate can be obtained analytically and a prediction can then be easily made. However,²¹ the approximation made by Gent and Wang grossly overestimates G and does not extrapolate to the correct solution in the linear regime. Alternatively, if the Griffith criterion is used to predict fracture initiation, Gent's result underestimates the critical hydrostatic stress P_c for crack initiation.

Lin and Hui,²¹ motivated by Gent and Wang's analysis, developed a more accurate way to calculate G by simulating a volume controlled expansion test with a finite element method using the exponentially hardening model optimized on PU8000 behavior.

The principle of the calculation is the following.

Initially the crack has a radius of r_0 . Using the definition of fracture energy,

$$G = \frac{1}{2\pi r_0} \left. \frac{\partial W}{\partial r_0} \right|_v \quad (7)$$

where W is the strain energy of the system, P is the hydrostatic stress, and V is the volume. It can be shown that for such a penny-shaped crack being inflated, G can be written as follows:

$$G = \frac{3}{2\pi r_0^2} \int_0^P V(P') dP' \quad (8)$$

where $V(P')$ is the deformed volume of the crack subjected to the internal pressure P' .

The reason to use eq 8 to determine the energy release rate is because it only requires the volume of deformed crack instead of the local stress field near the crack tip. It is easier to obtain the displacement field than the stress field with FEM method and the result for displacement fields is also more accurate.

Using the methodology of Lin and Hui,²¹ Long and Hui investigated the effect of triaxiality on the crack growth for strain hardening hyperelastic materials³⁰ and we use here their results and compare them with the experimental results obtained on the model elastomers.

The "adjustable" parameters are G_c and r_0 , where G_c can either be a threshold value of the G_{IC} as suggested implicitly by Gent and Wang,²⁰ or an experimentally determined value G_{IC} (in mode I by DENT) at the test temperature. Adjusting the r_0 value to get the best agreement between experimental data at 100 °C and model [see Fig. 12(a,b)] gives a value of $r_0 = 8 \mu\text{m}$. If a temperature independent threshold fracture energy is chosen as $G_c \cong G_{IC}$ (DENT) at $T = 100 \text{ }^\circ\text{C}$ [Fig. 12(b)] the data can clearly not fit the model.

However, if G_c is taken as G_{IC} (DENT) at the temperature where the cavitation tests were carried out, we observe an excellent agreement between data and model [see Fig. 12(c,d)], particularly knowing that only the theoretical curve for the PU8000 is precisely known and shown in the figure.

This very interesting result suggests that cavitation resistance is controlled not only by E but also by G_c and the methodology to model cavitation in crosslinked rubbers proposed by Gent and Wang²⁰ in 1991 is inherently correct if G_c is taken as the mode I fracture toughness of the elastomer at a

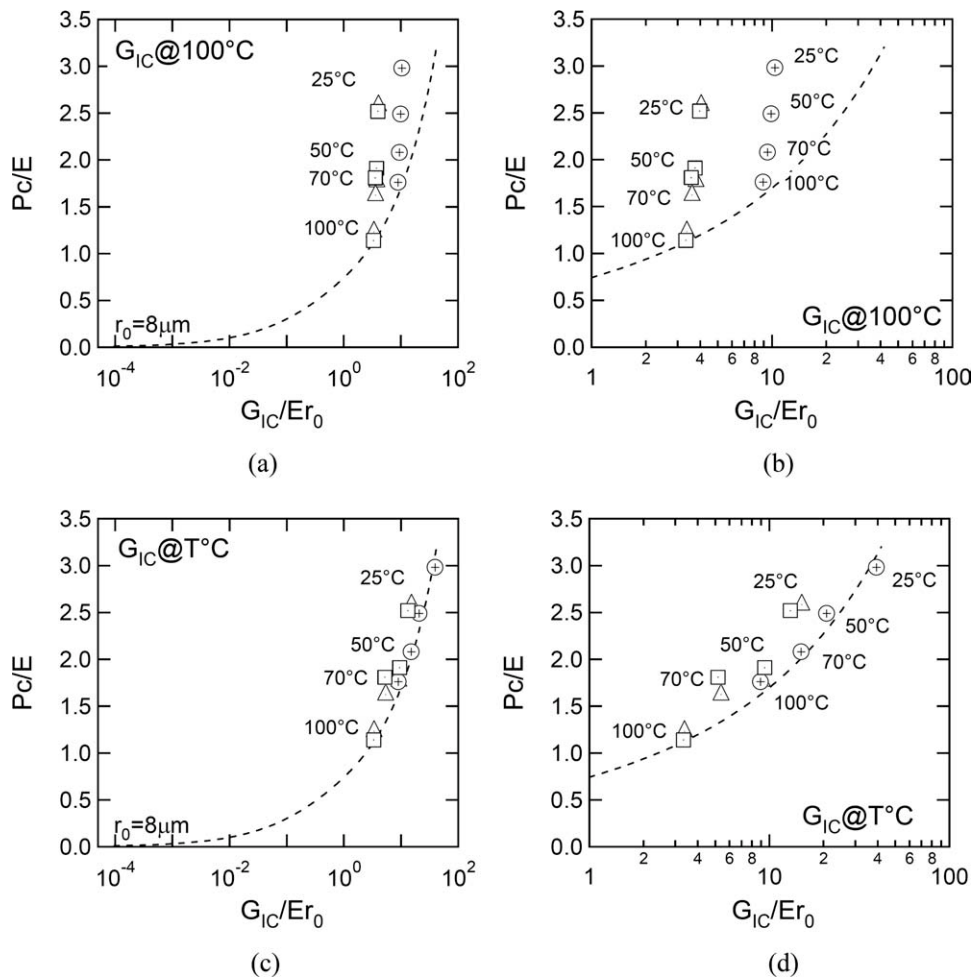


FIGURE 12 Fits of our experimental data to the curves predicted from the FEM simulations for the PU8000 (dashed lines) using $r_0 = 8 \mu\text{m}$ and the material parameters of Table 4: (a) using $G_0 \cong G_c$ at highest temperature, (b) zoom using $G_0 \cong G_c$ at highest temperature, (c) using G_c at different temperatures, and (d) zoom, using G_c at different temperatures. \circ PU8000, \square PU4000, and Δ PU8000-1000.

similar strain rate. To our knowledge, we present here the first clear experimental verification of this model.

Furthermore, the data on Figure 12(d) implies that a more pronounced and steeper strain hardening for the PU8000/1000 and for the PU4000 would lead to a better fit of the data. Unfortunately, these two networks were too brittle to be reliably characterized in the strain hardening region of the stress/strain curve and this point could not be checked.

GENERAL DISCUSSION

Although our results are unambiguous, there are several points that deserve further discussion.

The most important is the role played by the fracture energy in controlling the resistance to cavitation. The classic results of Gent and Lindley were not obtained at different temperatures but with different materials.¹⁵ They clearly showed using a poker-chip geometry that the measured “yield” stress was proportional to the elastic modulus of the rubber. Our

results suggest that the mode I G_c of their materials probably also increased with E . This point requires further investigation with a variety of different filled and unfilled elastomers. It is in particular unlikely that the G_{IC} value of filled elastomers, which can reach very high values, is the main parameter controlling the cavitation strength for filled rubbers.

The effect of strain rate has not been investigated here but previous studies have shown that soft materials are prone to time-dependent failure under stress.³¹ It is not clear here what would have been the effect of decreasing the strain rate or maintaining a constant stress on the crack nucleation process.

A more fundamental question that arises is why is it possible to fit the data for all temperatures and for all three networks by using the same initial crack length r_0 . In other words, while there is probably an initial size distribution of defects in each sample, the critical stress for cavity growth which we have characterized with the macroscopic peak force, is a deterministic and reproducible value controlled by the

fracture toughness G_c and the modulus E of the rubber network but not by the distribution of initial sizes of defects r_0 . The question of the nature of the “defects” present in the elastomers is clearly a very important one. One can easily envision some heterogeneities due to the synthesis method but they should be at the molecular mesh level. Some larger (micron-size) defects due to impurities (dust, etc...) could also be present in the samples although we took care to minimize them. However, there is no reason that these larger defects should have to same size in all materials.

Therefore, it is likely that the fracture by cavitation occurs in two stages, a first stage where a small ($r < 8 \mu\text{m}$) defect grows in the material over time under hydrostatic stress, and a second stage where the now larger defect ($r \sim 8 \mu\text{m}$) expands by uncontrolled fracture. The reason why this particular size comes from the analysis of the data is presently unknown but it could be due to a finite size effect of the sample geometry we use.

CONCLUSIONS

We developed a new experimental geometry to study the nucleation and growth of cavities in confined elastomers. Although the so called “poker chip” (flat-to-flat) geometry has been the most reported in the literature, some practical aspects such as the control of the parallelism between the two plates are difficult to adjust and for this layer the multiple nucleation of cavities that is observed makes it difficult to relate stress values with cavity growth. Our sphere-to-flat geometry with an aspect ratio $a/h = 10/1$ allowed us to observe most of the time one single cavity/crack growing very close to the center of the sample and never at the interface and hence correlate precisely cavity growth and stress/time curves.

The simple cavity deformation model used in earlier studies¹⁵ predicting a cavitation strength increasing linearly with the modulus E did not fit at all our experimental results obtained for a given material at different temperatures. The cavitation strength for a given elastomer is clearly controlled by both its modulus and its fracture toughness in mode I G_{IC} as predicted by more recent models.^{20,21} The ratio G_{IC}/E defines a length scale which varied between 25 and 320 μm depending on the temperature and material. It could be interpreted as a limit of stability of an existing crack (determined with the linear theory).

Using a penny-shape precursor crack in an infinite medium as an idealized geometry and a nonlinear constitutive model, we were able to predict G as a function of initial crack size and nonlinear elastic properties of the rubber. This model was able to properly fit the experimental data by using a constant value of the initial crack size r_0 and the G_{IC} value for the networks obtained in mode I (DENT geometry) at the test temperature.

The successful predictions of the model suggest that cavitation strength can be improved by increasing the mode I fracture toughness and the degree of strain hardening.

Finally, in our model materials, the network with the longest chains (entangled) was clearly tougher in mode I but also the most resistant to cavitation relative to its elastic modulus. The introduction of 20 wt % of very short chains ($M_n = 1 \text{ kg/mol}$) in a network of long ($M_n = 8 \text{ kg/mol}$) chains did result in a slightly higher cavitation strength but also embrittled the material and increased its small strain modulus significantly.

The authors like to specifically thank Bert Keestra, Paul Steeman, and Markus Bulters from DSM research for numerous helpful discussions and for the financial support. They also like to thank Lucien Laiarinandrasana (ENSMP) for helpful discussions and Ludovic Olanier for the design and construction of the samples'holder, metallic molds, and teflon molds. Chung Yuen Hui and Rong Long are supported by the Department of Energy, Office of Basic Energy Sciences, Division of Material Sciences and Engineering under award no. DE-FG02-07ER46463.

REFERENCES AND NOTES

- Gent, A. N. *Rubber Chem Technol* 1990, 63, G49–G53.
- Ball, J. M. *Philos Trans R Soc Lond A* 1982, 306, 557–611.
- Biwa, S. *Int J Non Linear Mech* 2006, 41, 1084–1094.
- Chang, W. J.; Pan, J. *J Mater Sci* 2001, 36, 1901–1909.
- Dollhofer, J.; Chiche, A.; Muralidharan, V.; Creton, C.; Hui, C. Y. *Int J Solids Struct* 2004, 41, 6111–6127.
- Fond, C. *J Polym Sci Part B: Polym Phys* 2001, 39, 2081–2096.
- Ganghoffer, J. F.; Schultz, J. *Rubber Chem Technol* 1995, 68, 757–772.
- Horgan, C. O.; Polignone, D. A. *Appl Mech Rev* 1995, 48, 471–485.
- Hou, H. S.; Abeyaratne, R. *J Mech Phys Solids* 1992, 40, 571–592.
- Lopez-Pamies, O. *J Elast* 2009, 94, 115–145.
- Polignone, D. A.; Horgan, C. O. *J Elast* 1993, 33, 27–65.
- Volokh, K. Y. *Int J Solids Struct* 2007, 44, 5043–5055.
- Yerzley, F. L. *Ind Eng Chem* 1939, 31, 950–956.
- Busse, W. F. *J Appl Phys* 1938, 9, 438–451.
- Gent, A. N.; Lindley, P. B. *Proc R Soc Lond A Math Phys Sci* 1959, 249A, 195–205.
- Green, A. E.; Zerna. *Theoretical Elasticity*; Oxford University Press: Oxford, 1954.
- Cho, K.; Gent, A. N. *J Mater Sci* 1988, 23, 141–144.
- Oberth, A. E.; Bruenner, R. S. *Trans Soc Rheol* 1965, 9, 165–185.
- Oberth, A. E. *Rubber Chem Technol* 1967, 40, 1337–1363.
- Gent, A. N.; Wang, C. *J Mater Sci* 1991, 26, 3392–3395.

- 21** Lin, Y. Y.; Hui, C. Y. *Int J Fract* 2004, 126, 205–221.
- 22** Bos, H. L.; Nusselder, J. J. H. *Polymer* 1994, 35, 2793–2799.
- 23** Cristiano, A.; Marcellan, A.; Creton, C. to be published.
- 24** Rubinstein, M.; Panyukov, S. *Macromolecules* 2002, 35, 6670–6886.
- 25** Seitz, M. E.; Martina, D.; Baumberger, T.; Krishnan, V. R.; Hui, C.-Y.; Shull, K. R. *Soft Matter* 2009, 5, 447–456.
- 26** Gent, A. N. *Rubber Chem Technol* 1996, 69, 59–61.
- 27** Lake, G. J.; Lindley, P. B. *J Appl Polym Sci* 1965, 9, 1233–1251.
- 28** Gent, A. N. *Rubber Chem Technol* 1994, 67, 549–558.
- 29** Griffith, A. A. *Philos Trans R Soc Lond A* 1920, A221, 163–198.
- 30** Long, R.; Hui, C. Y. *Soft Matter* 2010, 6, 1238–1245.
- 31** Bonn, D.; Kellay, H.; Prochnow, M.; Ben-Djemaa, K.; Meunier, J. *Science* 1998, 280, 265–267.